Comparative Three-Dimensional Finite-Element Assessment of Settlement-Induced Tensile Demand and Grouting Uplift in Airport Concrete Pavement Slabs

Xin Xin

HEILONGJIANG COMMUNICATIONS PLANNING AND DESIGN INSTITUTE GROUP CO.LTD, 90 Qingbin Road, Nangang District, Harbin, 150086, China
2410990425@qq.com

Abstract. Differential settlement and loss of support beneath airport concrete pavement slabs may require corrective grouting during different maintenance stages. In this study, two complementary three-dimensional models were developed, including a 3 × 3 slab array model with prescribed Gaussian settlement and an independent layered model with predefined grouting-induced uplift zones. Under a fixed settlement radius of 1.5 m, increasing the maximum settlement from 2 mm to 4 mm approximately doubled the nominal linear-elastic tensile-demand index, which is interpreted only as a relative severity indicator because the calculated values exceed the assumed tensile strength of concrete. For central injection, increasing the effective diameter from 0.5 m to 2.0 m reduced the critical uplift pressure from 5.54 MPa to 0.38 MPa, while the corresponding total uplift force remained within a similar range. The calculated uplift displacement of 15.7–18.0 mm was within the same displacement scale as the reported field value of 17.0 mm, providing a preliminary field-case consistency check. The results highlight the importance of considering injection position and effective uplift area when interpreting grouting-induced slab responses within the adopted linear-elastic framework.

Keywords: Airport Concrete Pavement, Grouting Uplift, Subgrade Settlement, Finite Element Analysis, Critical Uplift Pressure, Pressure Control.

1 Introduction

Rigid airport pavements need to have proper and uniform support. Due to factors such as water infiltration, voids or uneven settlement occur, and the concrete slab becomes a local spanning member, which will increase deflection, cause tensile conditions, and damage at edges and corners [1-4]. Pore pressure under saturated conditions will accelerate the erosion process [5]. Research carried out by airports shows that the load transfer between adjacent slabs and joints needs to be considered [6, 7].

Grouting can fill voids, restore support, and make the settlement plate rise again, and there is no need for full-depth replacement. However, unexpected movement is a difficult problem in construction [8]. In material research, emphasis is placed on fluidity,

© The Author(s) 2026
H. Wu et al. (eds.), *Proceedings of the 2026 3rd International Conference on Civil Engineering Structures and Concrete Materials (CESCM 2026)*, Advances in Engineering Research 312,
https://doi.org/10.2991/978-94-6239-865-8_10

solidification conditions, strength performance, and expansion phenomena [9, 10]. For the structural aspect, it is also necessary to consider the pressure margin conditions at the center, edge, and corner of the plate.

Recently, FEM - DEM coupling has been integrated into the work to describe pore generation and grouting reinforcement [11], and data has been used to drive pore prediction [12]. Existing studies have mainly focused on grout material properties and repair effectiveness, whereas the relationship between settlement characteristics, injection configuration and slab response under a consistent numerical framework remains insufficiently understood.

This article puts forward two complementary analysis methods, which belong to the non - sequential coupling situation. The plate array model is used to test the specified settlement and uplift limits corresponding to different injection positions and diameters; compare the separate layer model with the lifting conditions recorded by airport panels to clarify the trend of injection layout and pressure control. The relevant content about the flow of cement slurry is not involved at present.

2 Nominal Linear-elastic Tensile-demand Index State of Pavement Slabs Induced by Subgrade Settlement

2.1 Geometry, Material Properties and Boundary Conditions

Nine 5.0 m by 5.0 m by 0.40 m slabs formed a 3 × 3 array, with the center slab as the analysis object (Fig. 1a). A circular surface beneath it represented settlement. The regular outer slabs used swept hexahedral elements and the center region used a refined tetrahedral mesh. The source project record did not include a formal mesh-convergence study; consequently, the results are interpreted as comparative parametric trends. Settlement followed a Gaussian surface (Fig. 1b), while a separate layered model was used for the field-case uplift calculation (Fig. 1c). Hexahedral elements were used in the regular outer regions, whereas a locally refined tetrahedral mesh was adopted around the irregular settlement or injection zones. Identical meshing criteria were maintained for all cases within each parametric series to ensure a consistent basis for comparison.

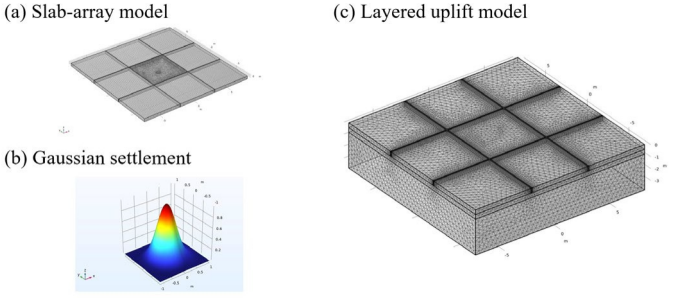


Fig. 1. Numerical models and settlement input: (a) 3 × 3 slab array, (b) Gaussian settlement surface and (c) layered pavement-base-subgrade model.

Before concrete cracks, it is in a linear elastic state. The load transfer efficiency of the 0.01 - meter virtual joint in the original model reaches 0.9. The outer edge is supported by rollers. The foundation subgrade is simulated and supported by distributed springs. After the self - weight reaches equilibrium, a specified displacement is applied to the springs in the defective area. Since it is calculating the situation of closing the road surface during diagnosis and maintenance, the aircraft wheel load is not considered:

$$T(x,y) = a\,exp(-((x - x_0)^2 + (y - y_0)^2)/(2c^2)) \quad (1)$$

where (x_0, y_0) is the settlement center, a is maximum settlement and c controls Gaussian decay. The effective radius r defines the circular working surface over which the displacement is prescribed. The depth series used r = 1.5 m and a = 2, 3 and 4 mm; the radius series used a = 2 mm and r = 1.0, 1.5 and 2.0 m. The same support and joint parameters were used in every comparison. Table 1 lists the material properties.

Table 1. Material properties in the slab-array model.

Material	Density (kg/m³)	Elastic modulus (MPa)	Poisson's ratio	Tensile strength (MPa)
C40 concrete	2500	35,000	0.15	4.5
Virtual joint	500	600	0.30	-

2.2 Mesh Configuration and Result Interpretation

Hexahedral elements were used in the regular outer regions, whereas a locally refined tetrahedral mesh was adopted around the irregular settlement or injection zones. Identical meshing criteria were maintained for all cases within each parametric series to ensure a consistent basis for comparison. To avoid overinterpretation of localized numerical concentrations, the assessment emphasizes centerline response profiles and relative variations among cases rather than isolated nodal peaks. The reported stress values are therefore interpreted as nominal elastic demand indices within the adopted discretization and are not proposed as direct design stresses.

2.3 Effects Of Settlement Depth and Radius

Figure 2 shows the nominal linear-elastic tensile-demand index and displacement conditions at the center line. When fixed at the position of 1.5m radius, when the maximum settlement reaches 2mm, 3mm, and 4mm, the nominal line elastic bottom tensile nominal linear-elastic tensile-demand index index of the plate is 48.5MPa, 73.4MPa, and 97.2MPa respectively, showing an almost linear growth trend, with approximately 24.4MPa change in the tensile nominal linear-elastic tensile-demand index index per millimeter. The tensile strength with three peaks exceeding 4.5MPa means that the specified deformation causes actual plate rupture rather than interpreting it as the nominal linear-elastic tensile-demand index after rupture or predicting the crack width.

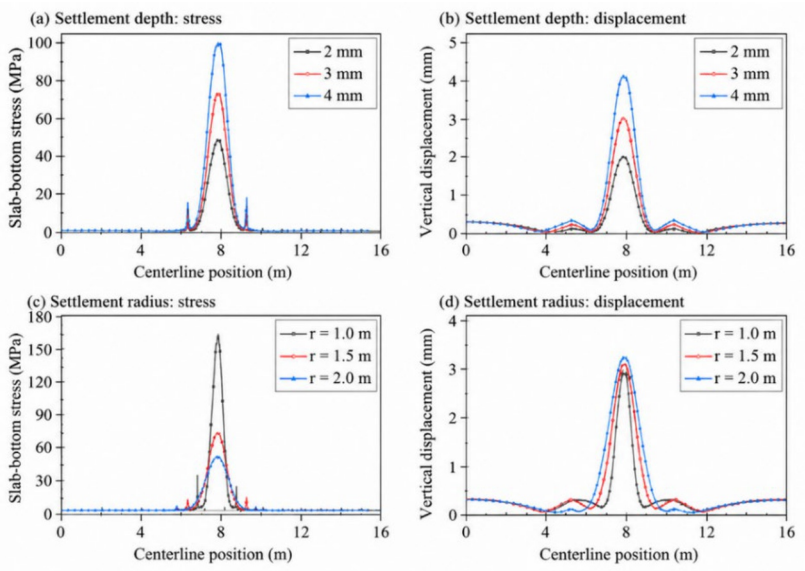


Fig. 2. Centerline responses caused by subgrade settlement: effects of maximum settlement depth on (a) nominal elastic nominal linear-elastic tensile-demand index index and (b) vertical displacement, and effects of settlement radius on (c) nominal elastic nominal linear-elastic tensile-demand index index and (d) vertical displacement.

The computed tensile-demand indices exceed the assumed concrete tensile strength for all prescribed settlement cases. This exceedance indicates that the linear-elastic state would terminate at crack initiation; values beyond this point must not be interpreted as physical post-cracking stresses. They are retained only as nominal elastic indices for comparing the influence of settlement depth and radius. After cracking, stiffness degradation and stress redistribution would alter the local stress field, deflection pattern, crack path and residual capacity. Quantifying these responses requires a fracture-energy-based nonlinear formulation and is outside the scope of the present comparative analysis.

3 Three-Dimensional Simulation of Grouting Uplift

3.1 Critical Uplift Pressure and Analysis Cases

In the independent uplift analysis, the geometric form of the plate array is repeatedly applied; the pre-settlement deformation or nominal linear-elastic tensile-demand index is not preset before. After the system achieves self-weight balance, the regional foundation springs are moved and injected, and uniform upward pressure is applied to the space according to the rules of the numerical loading step. The maximum first principal tensile nominal linear-elastic tensile-demand index is tracked through the probe, and the loading is stopped when the nominal linear-elastic tensile-demand index reaches the tensile strength of 4.5 MPa. The corresponding pressure at this time is the critical

uplift pressure. Central injection operations are carried out on circles with diameters of 0.5 meters, 1.0 meter, and 2.0 meters respectively. Then, the situation of the 0.5-meter diameter is compared with the center, edge, and corner injection conditions of the slab.

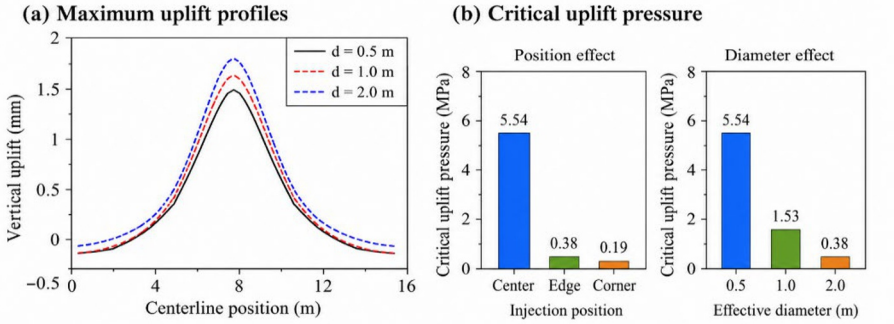


Fig. 3. Influence of injection range and position: (a) centerline uplift profiles at the maximum analyzed states and (b) critical uplift pressure for injection position and effective diameter.

When the effective diameter increases, the maximum uplift first increases and then slightly decreases, and the footprint after deformation shows a widening trend (Figure 3a). When the diameters are 0.5 meters, 1.0 meter, and 2.0 meters, the critical pressures decrease from 5.54 MPa to 1.53 MPa and 0.38 MPa in turn. However, the total uplift pressure obtained by multiplying the pressure by the area of the circular active area is approximately 1.09, 1.20, 1.19 MN. The main reason for the decrease in diameter pressure is the distribution of large-area loads, not the proportional decrease in the total uplift pressure. When the diameter is 0.5 meters, the critical pressure decreases from 5.54 MPa at the center to 0.38 MPa at the edge and to 0.19 MPa at the corner, which means that the force margin near the free plate boundary is much smaller.

3.2 Representative Nominal Linear-Elastic Tensile-Demand Index Fields and Pressure-Area Interpretation

The representative first principal nominal linear-elastic tensile-demand index field shows that when the effective diameter increases, the nominal linear-elastic tensile-demand index area will expand, and the lifting situations are more widely distributed (as shown in Figure 4). This is consistent with the situation that the total uplift force is almost stable. Therefore, when there is no relevant effective area, it should not be compared with the pressure value. The place where Figure 3b is located is more sensitive. Within the same 0.5-meter area, the injection pressure and force margin at the edges and corners are smaller than those at the center. Therefore, more detailed monitoring of the pressure increment and close attention to the elevation situation are needed.

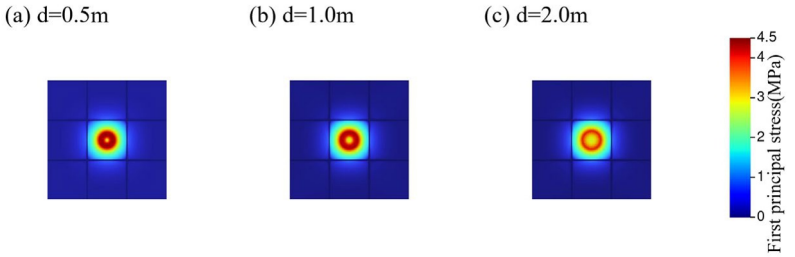


Fig. 4. First principal nominal linear-elastic tensile-demand index fields at the critical state for center injections with effective diameters of (a) 0.5 m, (b) 1.0 m and (c) 2.0 m.

3.3 Layered Model and Field Case

The second model contains a plate - like structural system of 3 by 3, a foundation part with a thickness of 0.40 meters, grouting or weak areas as well as subgrade construction. The size of the general plate is 5.0 meters in length, 5.0 meters in width and 0.40 meters in thickness, and they are separated by virtual joints of 0.01 meters. The weak areas in the initial state are shown as semi - ellipsoids with main dimensions of 1.5 meters, 1.0 meter and 0.5 meter respectively. The bottom end of the subgrade is fixed, and the transverse edges are supported by rollers. Since there is no pressure - related grout diffusion situation or measurement reaction law, the action of the grout is reflected by the dimensionless prescribed expansion parameter, which linearly increases to 0.20 in the loading step, and it is the equivalent intrinsic expansion input, not the measured material expansion ratio or physical construction time. The material properties and thicknesses of the pavement and subgrade layers used in the field-case model are summarized in Table 2.

There is a case on site, which is Group 12 of a settled area in Daxing Airport. The maximum edge here has a settlement of 32 mm, and after grouting treatment, there is a stable uplift phenomenon of 17 mm. It is repaired by using two lifting holes and seven stable holes (see Figure 5). The record on site shows that the amount of cement slurry poured into each lifting hole is about four times that of the stable hole. When constructing the hemisphere, the effective radius makes the lifting hole reach 0.79 meters and the stable hole reach 0.50 meters.

Table 2. Layer properties used for the Panel 12 field-case model.

Layer	Thickness (m)	Density (kg/m³)	Elastic modulus (MPa)	Poisson's ratio
PCC surface	0.44	2300	30,000	0.20
Cement-treated base	0.40	2200	1700	0.25
Subgrade	2.00	2000	40	0.30

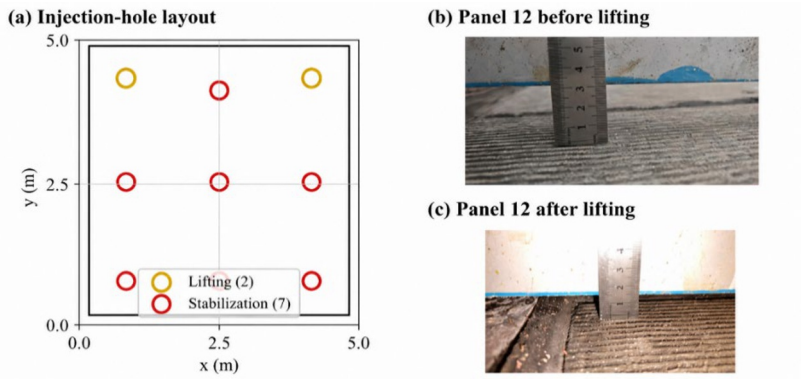


Fig. 5. Field case: (a) arrangement of two lifting holes and seven stabilization holes, (b) Panel 12 before lifting and (c) Panel 12 after lifting.

3.4 Spatial Uplift Response and Field-Case Comparison

The modeled grout zones and report-derived spatial profiles are summarized in Fig. 6. Calculated uplift was greatest near the concentrated grout zones and decayed with distance. The calculated center uplift was approximately 18.0 mm and the edge uplift near the lifting holes was 15.7 mm. Relative to the single reported stabilized uplift of 17.0 mm, these values differ by +5.9% and −7.6%, respectively. Because a point-by-point field elevation map and pressure-volume history were unavailable, this agreement is a plausibility check for the displacement scale, not an independent field-case consistency check of grout pressure, diffusion or the spatial uplift field.

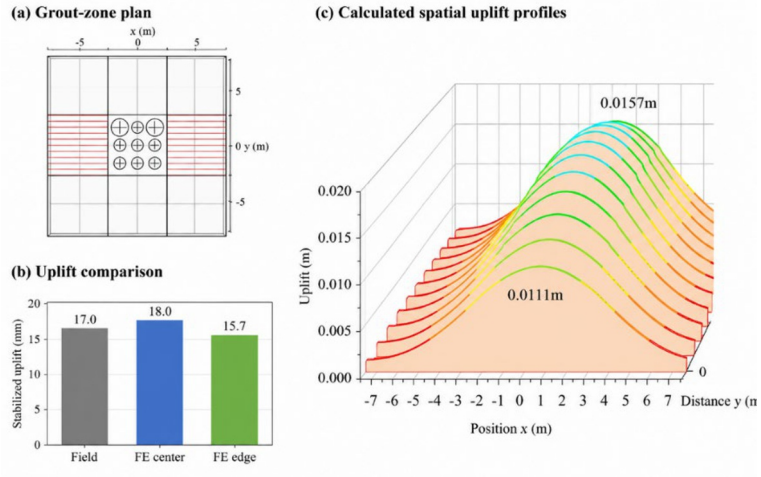


Fig. 6. Field-case comparison using report-backed information: (a) modeled grout-zone plan, (b) comparison of the reported stabilized uplift with calculated center and edge values and (c) calculated spatial uplift profiles.

3.5 Engineering Implications and Limitations

The results suggest that settlement geometry or void distribution should be identified before grouting to determine regions with lower uplift resistance, especially near slab edges and corners. A position-dependent grouting strategy with controlled pressure can be adopted to gradually restore uniform support conditions. Monitoring injected volume, pressure, effective grouting area, and uplift force provides preliminary guidance for optimizing grouting layout and pressure management, thereby improving support conditions and load-transfer performance [8].

The simulation presentations of settlement and uplift are complementary, not coupled in sequence. The two models are in a linear elastic state, and the redistribution situation after cracking cannot be reflected. The source project lacks a formal grid convergence exploration, and there is no calibration of the support stiffness and clear node contact situation. The opening at the joint, etc., is simplified; the expansion situation during grouting is clearly specified, not caused by factors such as coupled flow, etc.; except for the case of aircraft loading; the displacement situation reported on site is different from the situation of using a single panel. These limitations make the results only meaningful in comparing the development trend of mechanics and carrying out preliminary construction control.

4 Conclusions

Two complementary three-dimensional analyses were used to examine prescribed settlement and grouting-induced uplift. Within the stated assumptions, the principal findings are:

1. Under the adopted linear-elastic discretization, increasing the prescribed settlement from 2 to 4 mm increased the nominal slab-bottom tensile-demand index. Because the calculated indices exceed the assumed tensile strength, the defensible interpretation is limited to the relative increase in crack-initiation tendency within the adopted linear-elastic framework, rather than a quantitative prediction of post-cracking stress or damage.
2. The critical uplift pressure varies at different positions. For the same area with a diameter of 0.5 meters, the critical uplift pressure at the center of the plate reaches 5.54 MPa, at the edge position it is 0.38 MPa, and at the corner part it is 0.19 MPa. It can be found that the control margin is relatively small near the free boundary.
3. For center injections, increasing effective diameter from 0.5 to 2.0 m reduced critical pressure from 5.54 to 0.38 MPa, but the equivalent total uplift force remained about 1.09–1.20 MN. Pressure and active area should therefore be controlled jointly.
4. he field-case model produced 15.7–18.0 mm uplift compared with one reported stabilized value of 17.0 mm. This falls within the same displacement scale as the single reported field value. A stabilization-plus-lifting layout with incremental, position-dependent control is recommended for further field verification.

Disclosure of Interests. The author declares no competing interests.

References

1. Federal Aviation Administration: Airport Pavement Design and Evaluation. Advisory Circular AC 150/5320-6G, Washington, DC (2021).
2. Xu, C., Cebon, D.: Foundation voiding in jointed plain concrete pavements. J. Eng. Mech. 143(6), 04017018 (2017). https://doi.org/10.1061/(ASCE)EM.1943-7889.0001209.
3. Liu, B., Zhou, Y., Gu, L., Huang, X.: Finite element simulation and multi-factor nominal linear-elastic tensile-demand index prediction model for cement concrete pavement considering void under slab. Materials 13(22), 5294 (2020). https://doi.org/10.3390/ma13225294
4. Liu, B., Zhou, Y., Gu, L., Wang, D., Huang, X., Li, L.: Mechanical behavior of concrete pavement considering void beneath slabs and joints LTE. Adv. Civ. Eng. 2020, 8826301 (2020). https://doi.org/10.1155/2020/8826301.
5. Liang, K., Zeng, X., Ali, S., Li, X.: Hydrodynamic pressure distribution in saturated void beneath cement concrete pavement slab. Int. J. Pavement Eng. 23(5), 1413-1421 (2022). https://doi.org/10.1080/10298436.2020.1804064.
6. Wang, X., Ma, Z., Hu, X., Cao, X., Dong, Q.: Void detection of airport concrete pavement slabs based on vibration response under moving load. Sensors 25(15), 4703 (2025). https://doi.org/10.3390/s25154703.
7. Jamieson, S., White, G.: Validating a finite element model for rigid aircraft pavement load transfer against full scale testing. Int. J. Pavement Eng. 25(1), 2363943 (2024). https://doi.org/10.1080/10298436.2024.2363943.
8. Vennapusa, P.K.R., Zhang, Y., White, D.J.: Comparison of pavement slab stabilization using cementitious grout and injected polyurethane foam. J. Perform. Constr. Facil. 30(6), 04016091 (2016). https://doi.org/10.1061/(ASCE)CF.1943-5509.0000916.
9. Hu, C., Shi, S.: Summary of the grouting material for the void beneath cement concrete pavement slab. IOP Conf. Ser. Mater. Sci. Eng. 382, 022096 (2018). https://doi.org/10.1088/1757-899X/382/2/022096.
10. Huang, S., Li, C., Zhang, Z.: Design and performance evaluation of a cementitious repair grouting mortar for cement pavement slab cavity. Buildings 14(12), 4083 (2024). https://doi.org/10.3390/buildings14124083.
11. Zhang, X., Long, J., Wang, Z., Wang, Y., Ran, D.: Macro-micro mechanisms of void formation and grouting strength reinforcement in concrete pavement slabs using FEM-DEM coupling method. Sci. Rep. 15, 36938 (2025). https://doi.org/10.1038/s41598-025-20825-w
12. Shi, B., Qiao, D.: Prediction of void beneath concrete slabs based on FEM-ANN framework. In: Advances in Materials and Pavement Performance Prediction IV, pp. 575-578 (2025). https://doi.org/10.34726/10640.

Open Access This chapter is licensed under the terms of the Creative Commons Attribution-NonCommercial 4.0 International License (http://creativecommons.org/licenses/by-nc/4.0/), which permits any noncommercial use, sharing, adaptation, distribution and reproduction in any medium or format, as long as you give appropriate credit to the original author(s) and the source, provide a link to the Creative Commons license and indicate if changes were made.

The images or other third party material in this chapter are included in the chapter's Creative Commons license, unless indicated otherwise in a credit line to the material. If material is not included in the chapter's Creative Commons license and your intended use is not permitted by statutory regulation or exceeds the permitted use, you will need to obtain permission directly from the copyright holder.

